

# Edge instability regimes with applications to blob transport and the quasi-coherent mode

J. R. Myra and D. A. D'Ippolito

*Lodestar Research Corp., Boulder, Colorado 80301*

May 2005  
submitted to Phys. Plasmas

---

DOE/ER/54392-31

LRC-05-105

---

**LODESTAR RESEARCH CORPORATION**  
*2400 Central Avenue*  
*Boulder, Colorado 80301*

# Edge instability regimes with applications to blob transport and the quasi-coherent mode

J. R. Myra and D. A. D'Ippolito

*Lodestar Research Corp., 2400 Central Ave. P-5, Boulder, Colorado 80301*

## Abstract

An analytic theory of the resistive X-point (RX) mode in the edge region of a diverted tokamak is developed by employing an outgoing-evanescent wave boundary condition along the field lines. This result is employed to deduce a new categorization of edge instabilities in the presence of X-points. A regime diagram shows the relationship of the RX mode to the ideal and conventional resistive ballooning modes. In addition to describing growth rates of linear instabilities, the analysis also yields regimes and scalings for nonlinear convective “blob” propagation velocities. The regime diagram and a knowledge of experimental and BOUT code simulation results, suggests that the quasi-coherent mode seen in the Alcator C-Mod tokamak [M. Greenwald *et al.*, Phys. Plasmas **6**, 1943 (1999)] can be classified as an electromagnetic RX mode. Analytical scalings for the existence of this mode compare well with experimental trends, as does the solution of a model radial eigenvalue problem. Finally, using a finite Larmor radius assumption to eliminate the perpendicular wavenumber, the instability regime diagram can be converted to an edge phase space diagram. X-point physics adds a new region to this edge parameter space that is postulated to be the enhanced D-alpha (EDA) regime.

PACS: 52.55.Fa, 52.35.-g, 52.35.Qz

## I. Introduction

The importance of edge physics for the success of the tokamak fusion effort is being increasingly recognized. Large simulation codes will likely play a dominant role in exploring the nonlinear physics of edge turbulence and transport. In this environment, simple analytical models to clarify edge instability parameter regimes, and identify important transitions in parameter space, will fill a critical need for verifying code behavior, elucidating the underlying physics, and identifying promising regimes for experiments and simulations to explore. The goal of this paper is to present such a model for curvature-driven instabilities in the collisional edge and scrape-off-layer region of a diverted tokamak. The focus will be to clarify the role of X-points on edge instabilities, and note the implications of X-point physics for understanding the quasi-coherent mode observed in the Alcator C-Mod tokamak.<sup>1-3</sup> The model may also be relevant to certain types of quasi-coherent mode activity observed on DIII-D<sup>4</sup> and other tokamaks during quiescent periods in high-performance discharges.

Figure 1 illustrates schematically the basic instability physics under consideration. Curvature drives charge separation and currents flow in response. The instability regime is controlled by the topology of the resulting current loops, i.e. where they close. Possibilities include closure of the current at an end sheath [if the field line is in the scrape-off-layer (SOL)], or by perpendicular polarization currents near the midplane, or in the X-point region, where the flux tubes become thin elongated fans<sup>5</sup> and cross-field current flow is greatly eased. The path of least resistance will depend on the parallel resistivity as well as other parameters to be identified.

The conventional regimes of ideal strong ballooning (IB), resistive ballooning (RB) and connected (C) (or sheath-interchange, depending on whether the field lines are open or closed) are well understood and can be described by taking the extreme limits of

either localized or extended flute-interchange eigenfunctions along the field line. Instabilities whose properties depend on X-point geometry have also been studied,<sup>6-8</sup> but until now a simple analytical model description has not been available. This model and its implications are the subject of the present paper.

To understand the resistive X-point (RX) regime conceptually, we consider the model drift-resistive ballooning equation (see e.g. Ref. 6) for the perturbed potential  $\Phi \sim \exp(i\mathbf{k}\cdot\mathbf{x}-i\omega t)$

$$\frac{v_a^2}{k_\perp^2} \nabla_\parallel \frac{k_\perp^2 (\omega - \omega_{*e})}{\omega - \omega_{*e} + i\omega_\eta} \nabla_\parallel \Phi + \omega(\omega - \omega_{*i})\Phi + \gamma_{\text{mhd}}^2 \Phi = 0 \quad (1)$$

This equation is obtained from linearized equations of vorticity and continuity supplemented by a Braginskii-type Ohm's law and an Ampere's law. For simplicity, Eq. (1) neglects fluctuations in  $T_i$  and  $T_e$  and ignores electron inertia. The latter effect may be retained by the substitution  $i\omega_\eta \rightarrow i\omega_\eta + \omega(k_\perp \delta_e)^2$ . Furthermore, we work in the  $\mathbf{E} \times \mathbf{B}$  drift frame. Here, notations are standard and defined in full in Ref. 6. For convenience, we recall that  $v_a^2 = B^2/4\pi n m$  is the square of the Alfvén velocity,  $\omega_\eta = v_e(k_\perp \delta_e)^2$  is the magnetic diffusion frequency where  $\delta_e = c/\omega_{pe}$ ,  $\omega_{*j} = k_y v_{*j}$  ( $j = i, e$ ) are the species diamagnetic drift frequencies, and  $\gamma_{\text{mhd}}^2 \sim c_s^2/(RL_n)$  is the curvature drive. Occasionally we will use the notation  $x$  for radial, and  $y$  for binormal (approximately poloidal) projections, with  $k_\perp^2 = k_x^2 + k_y^2$ . In Eq. (1), it is well-known that  $k_\perp = k_\perp(s)$  due to magnetic shear and poloidal field variation (see for example Ref. 7 and references therein) where  $s$  is the coordinate along the magnetic field, and  $\nabla_\parallel = d/ds$ . Typically (for the fastest growing mode)  $k_\perp(s)$  has a minimum near the midplane and is a rapidly growing function.

The RX regime contrasts with the usual limits taken for resistive ballooning modes.<sup>9</sup> At the highest collisionalities or wavenumbers for which  $\omega_\eta \rightarrow \infty$ , the fast resistive modes are localized near the outboard midplane where the curvature term is

strongest. Consequently these modes do not experience the X-point region. These fast RB modes are susceptible to stabilization by diamagnetic effects, particularly in high performance tokamak plasmas. At lower collisionalities or wavenumbers, two-scale resistive ballooning models apply in *circular* flux surface geometry, and have been employed to describe edge modes.<sup>10</sup> The two-scale model relies on asymptotic matching in the extended ballooning coordinate  $\theta$ . However, the asymptotic region  $\theta \gg 1$  is seldom attained in X-point geometry because, as discussed subsequently, most modes decay on a single transit of the field line through the X-point region.

The important X-point physics in Eq. (1) comes from magnetic diffusion,  $\omega_\eta \sim \eta_{\parallel} k_{\perp}^2$ , and shear-enhanced ion polarization currents  $\sim k_{\perp}^2 (\omega - \omega_{*i})$ . Near the X-points, the local magnetic shear becomes large and the poloidal field becomes small,  $B_\theta \rightarrow 0$ , making  $\mathbf{k}_{\perp}$  a strong function of distance along  $\mathbf{B}$ .<sup>5</sup> The two-scale model for resistive ballooning modes fails and instead, the mode physics transitions suddenly (at  $\theta \sim 1$ ) from ideal to resistive. As  $\omega_\eta \propto k_{\perp}^2$  rises precipitously, the eigenfunction  $\Phi$  resistively disconnects at the X-points.<sup>7</sup> Examination of the parallel Poynting flux shows that wave energy propagates from the midplane region into the X-points.<sup>7</sup> This observation suggests the use of an outgoing wave boundary condition in the parallel direction. In Sec. II, we show how to employ a slight modification of a previously derived<sup>11</sup> outgoing-evanescent wave boundary condition to describe the essential X-point physics. This boundary condition enables an analytic theory of the RX mode in the radially local approximation and extends and clarifies previous numerical studies.<sup>6-8</sup>

In Sec. III, we employ this result to understand the competition of terms in the ballooning equation, *viz.* in what spatial regions (midplane or X-point) each term is important, as a function of wavenumber, collisionality and strength of the curvature drive. Balancing terms pair-wise gives the essential dimensionless parameters of our edge stability model, and determines regions in parameter space where transitions of the

dynamics can occur. These are identified first in a parameter space that includes wavenumber  $k_{\perp}$  for linear modes (or blob radius  $a_b$  for nonlinear convection). This allows comparison of RX and conventional resistive and ideal (RB and IB) ballooning modes and gives a general diagram illustrating the regimes where each mode is dominant. This diagram is useful for linear instabilities, but importantly also gives nonlinear blob propagation regimes, and scalings for blob convection velocities that can be tested experimentally. These are obtained by invoking a convective nonlinearity ansatz for the blobs.

In Sec. IV we make a postulate for the regime appropriate to the quasi-coherent (QC) mode, *viz.*, that it is a electromagnetic resistive X-point mode (RX-EM). Scalings are developed for its existence and compared with C-Mod experimental results. We also employ the theory to develop, then solve, a model radial eigenvalue equation for the QC mode.

Finally, in Sec. V, invoking finite Larmor radius (FLR) physics (i.e. diamagnetic drift stabilization) to eliminate  $k_{\perp}$ , the important dimensionless parameter transitions are converted to the  $(\alpha_{\text{mhd}}, \alpha_{\text{d}})$  edge phase space,<sup>12</sup> now including X-point effects. The result gives scalings which elucidate the QC mode and enhanced D-alpha (EDA) regimes. Our conclusions are summarized in Sec. VI.

## II. Analytic theory of resistive X-point modes

### *A. Outgoing-evanescent wave X-point model*

In Ref. 11, Ryutov and Cohen proposed the use of an outgoing-evanescent wave boundary condition to model X-point effects for instabilities localized to the divertor region. Here we make use of a similar idea, for the midplane-side RX modes, retaining diamagnetic drift physics and employing the cross-field ion polarization current (instead

of the collisional perpendicular electron conductivity used in Ref. 11) to close the current loops across the thin flux-tube fans of the X-point region. A related outgoing-evanescent wave model was employed earlier to show that drift-waves in X-point geometry are unstable,<sup>13</sup> in contrast with the circular-flux-surface result.

Our model has two regions along the field lines: the midplane region (in which all parameters in the ballooning equation are constant) and the X-point region. The midplane region, of half length  $L_{\parallel}$ , includes inertia, curvature drive, and parallel current (charge flow) and is described by integrating the ballooning equation along  $B$  from the midplane to the X-points to obtain

$$\omega(\omega - \omega_{*i}) + \gamma_{\text{mhd}}^2 + \frac{i\omega v_a}{k_{\perp}^2 \rho_s^2 L_{\parallel}} \left( \frac{J_{\parallel \text{bc}}}{\Phi} \right) = 0 \quad (2)$$

Here, the parallel current  $J_{\parallel}$  and potential  $\Phi$  are normalized to  $nev_a$  and  $T_e/e$  respectively.  $J_{\parallel \text{bc}}$  is the parallel current boundary condition connecting the midplane and X-point regions and is given, at the entrance to the X-point region by

$$\left( \frac{J_{\parallel \text{bc}}}{\Phi} \right) = \frac{-iv_a k_{\perp}^2 \rho_s^2 (\omega - \omega_{*e})}{\omega(\omega - \omega_{*e} + i\omega_{\eta})} \left( \frac{1}{\Phi} \nabla_{\parallel} \Phi \right) \quad (3)$$

The X-point region itself includes resistive line bending (with magnetic diffusion), and inertia (from the ion polarization current):

$$\frac{v_a^2}{k_{\perp}^2} \nabla_{\parallel} \frac{k_{\perp}^2 (\omega - \omega_{*e})}{\omega - \omega_{*e} + i\omega_{\eta}} \nabla_{\parallel} \Phi + \omega(\omega - \omega_{*i}) \Phi = 0 \quad (4)$$

This equation is solved for a model profile of  $k_{\perp}(s)$ , subject to the condition that solutions decay beyond the X-point. For validity of the fully disconnected limit,  $\Phi$  is assumed to vanish before reaching the divertor plate in the SOL, or before self-connecting around the tokamak on closed flux surfaces. This “disconnection” condition will be given in Eq. (8). Once Eq. (4) is solved in the X-point region,  $\nabla_{\parallel} \ln \Phi$  is computed at the entrance to the

X-point region, and substituted into Eq. (3). Equations (2) and (3) then give the dispersion relation for RX modes.

### ***B. Solution in the WKB limit***

Analytic solutions of Eq. (4) are possible in the Wentzel-Kramers-Brillouin (WKB) approximation, and in the “Born” limit. We present the WKB limit here, and consider the more complicated Born limit in Appendix A. Converting  $\nabla_{\parallel} \rightarrow ik_{\parallel}$  in Eq. (4), solving for  $k_{\parallel}$  and combining with Eqs. (2) and (3) one obtains the RX mode dispersion relation

$$\gamma_{\text{mhd}}^2 + i\omega_a \left( \frac{\omega(\omega - \omega_{*i})(\omega - \omega_{*e})}{\omega - \omega_{*e} + i\omega_{\eta}} \right)^{1/2} = 0 \quad (5)$$

Here,  $\omega_a = v_a/L_{\parallel}$  and midplane inertia  $\omega(\omega - \omega_{*i}) \ll \gamma_{\text{mhd}}^2$  has been dropped. Detailed analysis (not reproduced here) verifies that the unstable branches of Eq. (5) indeed correspond to legitimate (outgoing and/or evanescent) eigenmodes asymptotically in the X-point region for the consistent choices of the square root determining  $k_{\parallel}$ . All quantities here refer to *midplane* values (since they arise from the entrance to the X-point region). The WKB outgoing-evanescent wave boundary condition has no knowledge of properties interior to the X-point region: no interior information is transmitted back the midplane since there is no reflection in the WKB limit.

Equation (5) represents a mode driven by curvature from the midplane region balancing inertia from the X-point region. Typical growth rates scale as  $\omega \sim \gamma_{\text{mhd}}^2/\omega_a$  so that midplane inertia is negligible for  $\gamma_{\text{mhd}}^2/\omega_a^2 \ll 1$ , which we will see is one of the boundaries of the RX mode regime. The RX mode has two sub-limits. In the electromagnetic (RX-EM) limit,  $\omega_{\eta} \ll \omega$ , the boundary condition Eq. (3) describes an outgoing Alfvén wave, a limit considered previously for pellets<sup>14</sup> and blobs<sup>15</sup> and reduces to

$$\omega(\omega - \omega_{*i}) = -\frac{\gamma_{\text{mhd}}^4}{\omega_a^2} \quad (6)$$

In the opposite, electrostatic (RX-ES) limit,  $\omega_\eta \gg \omega$ , the X-point boundary condition reduces to that of an evanescent resistive ballooning mode, yielding the dispersion relation

$$\omega(\omega - \omega_{*e})(\omega - \omega_{*i}) = \frac{-i\gamma_{\text{mhd}}^4 \omega_\eta}{\omega_a^2} \quad (7)$$

### III. Edge instability and blob transport regimes

#### A. Linear instability regimes

In this section, we apply Eq. (1) for the ideal and resistive ballooning modes in the midplane region, and Eqs. (2) – (4) for the resistive X-point modes. The characteristic frequencies are  $\omega_\eta$ ,  $\gamma_{\text{mhd}}$ ,  $\omega_a$ , and  $\omega_{*j}$ . We begin by neglecting drift effects, re-introducing them later. Thus, the reduced system may be characterized by the dimensionless parameters  $X = \omega_\eta/\omega_a$  describing collisionality and wavenumber, and  $Y = (\gamma_{\text{mhd}}/\omega_a)^2$  describing the strength of the curvature drive. Again, in this section, all quantities refer to midplane values, unless otherwise noted.

In addition, there is a condition that the modes “disconnect” across the X-point region. In the WKB limit, this condition is

$$\int ds \text{Im} k_{\parallel}(s) > 1 \quad (8)$$

where the integral is taken across the X-point region, up to the divertor plate. Estimating  $k_{\parallel}$  from Eq. (4) and defining  $L_d$  to be the length of the integration region, the disconnection condition becomes

$$\frac{(\omega\omega_{\eta 0})^{1/2}}{\varepsilon_x \omega_a} > 1 \quad (9)$$

where

$$\varepsilon_x^{-1} = \frac{L_d}{L_{\parallel}} \left\langle \frac{k_{\perp}(s)}{k_{\perp 0}} \right\rangle \quad (10)$$

Here,  $\langle \dots \rangle$  indicates a field line average over the X-point-divertor region, and  $\omega_{\eta 0}$  in Eq. (9), and  $k_{\perp 0}$  in Eq. (10) emphasizes mid-plane values (i.e. entrance to the X-point region), although for notational consistency, we henceforth drop the subscript 0. The X-point geometry parameter  $\varepsilon_x$  is small for two reasons: (i) due the strong elliptical fanning of the X-point region,  $k_{\perp}$  is enhanced over its midplane value,<sup>5,6</sup> and (ii)  $L_d > L_{\parallel}$  (midplane length) since the separatrix geometry enhances the field line length in the vicinity of the X-point.

The dimensionless parameters X, Y, and  $\varepsilon_x$  completely characterize the solution space of instabilities in the model. Balancing terms pair-wise in each equation determines the behavior (e.g. dimensionless linear growth rate  $\hat{\omega} \sim \gamma/\omega_a$ ) in a given regime, while balancing terms in triplets gives the regime boundaries. We illustrate the procedure in detail for a few of the regimes, and summarize the results in Fig. 2 and Table 1.

The scalings for the ideal strong ballooning mode (IB) are obtained from Eq. (1) (in the midplane region) by balancing curvature drive with inertia (i.e. polarization current) to obtain  $\omega \sim \gamma_{\text{mhd}}$ . The first (i.e. line bending) term in Eq. (1) is negligible when  $(\gamma_{\text{mhd}}/\omega_a)^2 = Y \gg 1$ . This mode has the character of a standing Alfvén wave in the midplane region. The resistive strong ballooning mode (RB) similarly balances midplane inertia with curvature drive to obtain  $\omega \sim \gamma_{\text{mhd}}$ , but the first term in Eq. (1) is small in the RB regime because of large resistivity  $\omega_a^2/\omega_{\eta} \ll \gamma_{\text{mhd}}$ . Current loops close

locally in the midplane region for RB modes. These regimes illustrate how the conventional ballooning modes manifest themselves in our model.

For the RX modes, midplane curvature drive creates parallel currents to the X-point region, thus the  $\gamma_{\text{mhd}}$  and  $J_{\parallel\text{bc}}$  terms balance. We show *a posteriori* that the midplane inertial term is negligible. In the X-point region, inertial and line bending terms balance [see Eq. (4)]. Specifically, for the electrostatic RX-ES modes, ( $\omega_{\eta} \gg \omega$ ) current loops close by X-point polarization currents which balance resistive line bending in Eq. (4) and enable matching to an evanescent resistive ballooning mode. This limit was previously considered in the blob context<sup>16</sup> (see also the next sub-section). The linear growth rate, from Eq. (7), gives  $\omega \sim \gamma_{\text{mhd}}^{4/3} \omega_{\eta}^{1/3} / \omega_a^{2/3}$ . Thus, the resistive limit  $\omega_{\eta} \gg \omega$  applies when  $\gamma_{\text{mhd}}^2 \ll \omega_{\eta} \omega_a$  (i.e.  $Y \ll X$ ). Furthermore, midplane inertia is negligible in Eq. (2) when  $\omega \ll \gamma_{\text{mhd}}$ , which requires  $\gamma_{\text{mhd}} \omega_{\eta} < \omega_a^2$  (i.e.  $YX^2 \ll 1$ ), the condition defining the transition from the RX-ES to the RB regime. Finally, disconnection requires, from Eq. (9),  $\omega \omega_{\eta} \gg \varepsilon_x^2 \omega_a^2$  or  $\gamma_{\text{mhd}} \omega_{\eta} \gg \varepsilon_x^{3/2} \omega_a^2$  (i.e.  $YX^2 \gg \varepsilon_x^3$ ). These three boundaries enclose the region of parameter space for the RX-ES mode (see Fig. 2).

The properties and regime boundaries of the electromagnetic RX-EM mode are obtained similarly, using Eq. (6) to estimate  $\omega \sim \gamma_{\text{mhd}}^2 / \omega_a$ . In this case we have  $\omega_{\eta} \ll \omega$  and the midplane region sees an outgoing Alfvén wave condition, *viz.* the X-point is an absorbing boundary condition. The condition  $\omega_{\eta} \ll \omega$  gives  $Y \gg X$ ; neglect of midplane inertia gives  $Y \ll 1$ , separating the RX-EM modes from the ideal (IB) regime; while disconnection requires  $\gamma_{\text{mhd}}^2 \omega_{\eta} \gg \varepsilon_x^2 \omega_a^3$  (i.e.  $YX \gg \varepsilon_x^2$ ) provided that the WKB local growth rate estimate remains valid at these low values of  $k$ . These inequalities define the RX-EM regime in Fig. 2.

When the disconnection condition, Eq. (9) is violated, the mode remains finite throughout the X-point region. On closed field lines, such modes experience good

curvature on the inside of the torus, and become amenable to the standard two-scale resistive ballooning model mentioned in the introduction. On the open field lines in the SOL, the connected modes become sheath-interchange modes<sup>17</sup> with  $\omega \sim \gamma_{\text{mhd}}^2/\omega_s$  where the characteristic sheath frequency is  $\omega_s = c_s/(L_{\parallel}k_{\perp}^2\rho_s^2)$ .

Figure 2 illustrates the topology of the regimes in the (X, Y) plane. It may be verified that the characteristic growth rates of the ballooning (IB, RB) and RX modes are continuous across the regime boundaries. Note that the disconnection condition, and therefore the existence of the RX regimes, requires  $\varepsilon_x < 1$ ; otherwise, (e.g. for circular flux surface plasmas) on closed surfaces the strong (fast) resistive ballooning modes, and the ideal modes transition directly into the connected (slow two-scale) resistive and interchange modes. The scalings and boundaries of the regimes of Fig. 2 are also summarized in Table 1.

### ***B. Blob transport regimes***

Although the focus of the present paper is the linear physics and regimes of edge modes, it is useful to digress briefly and consider analogous regimes for convective “blob” transport. In blob theory,<sup>18,19</sup> semi-coherent convection of plasma in the SOL is achieved by balancing the time derivative with the convective derivative in the vorticity and continuity equations, so that a quasi-steady solution can be found in the convecting blob frame. Consequently, by estimating

$$\frac{\partial}{\partial t} \sim \mathbf{v} \cdot \nabla \quad (11)$$

linear growth rates can be mapped to the blob velocity (and hence to the charge-induced blob “polarization” potential  $\phi$ ). Thus, the regime diagram of Fig. 2 also gives the regimes and scaling of  $v_x$  for convective blob transport. The correspondences in going from linear modes to nonlinear blobs are summarized in Table 2, where  $a_b$  is the blob radius.

This correspondence is not inconsistent with the view that nonlinear saturation of turbulence by wave-breaking creates blobs which then propagate outwards. In this case the character of the blobs directly matches the underlying linear instability. However, it is also possible for different mechanisms and or regimes to dominate linear instability and blob creation on the one hand, and far SOL blob propagation on the other.

Some of the regimes indicated in Fig. 2 have been treated in the blob context, and in these cases, applying the correspondence rules of Table 2 recovers previously published results.<sup>20,21</sup> In the blob context, regime C is the sheath connected blob treated in the early blob papers.<sup>18,19</sup> The RX-EM regime corresponds to the Alfvén wave emitting blob<sup>14,15</sup> which may be related to edge localized modes (ELMs). The RX-ES regime is the three-dimensional (3-D) blob with current loop closure in the X-point region.<sup>16</sup> These blobs appear in 3-D turbulence simulations at high density<sup>16</sup> and may play a role in the density limit.<sup>20</sup> The RB regime corresponds to a two-dimensional (2-D) blob with local balance (at each point along the field line, in the plane perpendicular to B) between the ion polarization current and the curvature drive such as occurs for blobs smaller than a characteristic size.<sup>22</sup>

The analysis can therefore be used to obtain specific scalings of the radial convective velocity  $v_x \sim \phi/a_b$  for each regime. Since experiments cannot generally measure linear growth rates directly, the blob velocity scalings may provide a useful point of contact of the present theory with data. With the caveat that the present “hand-waving” analysis does not accurately predict order unity constants, the scalings are given in Table 3. In the last column of the table, we employ the dimensional units:  $v_x(\text{cm/s})$ ,  $n_e(\text{cm}^{-3})$ ,  $T_e(\text{eV})$ ,  $a_b(\text{cm})$ ,  $R(\text{cm})$ ,  $B(\text{G})$ , and  $q = L_{||}/R$ . For the numerical scalings, we have taken  $Z = 1$ ,  $\mu = 2$ , and  $\ln \Lambda = 15$  respectively for the ion charge ( $e$ ), ion/proton mass ratio and Coulomb logarithm. A sample scaling for sheath-connected thermalized density blobs in the collisionless limit (as treated in Refs. 18 and 19) is given; however,

other connected limits are also possible, including for example the effects of spin,<sup>23</sup> and parallel resistivity. A description of these regime boundaries would require additional dimensionless parameters, and is beyond the scope of the present analysis.

## IV. Application to the quasi-coherent mode and the EDA regime

### A. Postulate for the quasi-coherent mode

The present categorization of instability regimes, together with previous experimental results and simulations using the BOUT turbulence code<sup>24</sup> suggests that the QC mode observed on C-Mod is an RX-EM mode. This identification has specific implications for the plasma conditions required to support the mode when FLR (diamagnetic stabilization) considerations are invoked.

In each mode regime, there exists a  $k_*$  such that modes with  $k > k_*$  are stabilized by FLR, *viz.*

$$\omega_{*i} \equiv k_* v_{*i} = \gamma \quad (12)$$

where  $v_{*i}$  is the ion diamagnetic drift velocity, and  $\gamma$  the linear growth rate. As FLR effects increase, modes stabilize first at large  $X \propto k_\perp^2$ , then at increasingly smaller  $X$ . *Our postulate for existence of the QC mode and the EDA regime is that  $k_*$  lies in the RX-ES regime.* The reasons for, and implications of, this postulate will be the subject of the remainder of this section.

The postulated condition allows instability of all of the RX-EM modes while ensuring an FLR-stabilized RB branch. The stabilization of the RB branch was shown to be critical to suppressing strong turbulence associated with low-confinement-mode (L-mode) transport.<sup>12</sup> This RB suppression gives a second condition on the parameters and a window for the EDA regime, which we will return to in the next section. We first consider the condition that  $k_* = \omega/v_{*i}$  be larger than the  $k_\perp$  at the RX-ES/EM boundary

(i.e. the  $k_{\perp}$  defined by  $Y = X$ ),  $k_{\text{RX-ES/EM}} = \gamma_{\text{mhd}}/[\delta_e(v_e\omega_a)^{1/2}]$ . This condition may be expressed as

$$\gamma_{\text{mhd}}^2 \delta_e^2 v_e > \omega_a v_{*i}^2 \quad (13)$$

or equivalently

$$L_n v_e > R \omega_a \beta (m_i / m_e) \quad (14)$$

where  $L_n$  is the density gradient scale length,  $v_e$  is the electron collision frequency,  $\beta = c_s^2/v_a^2$  is the plasma beta, and  $m_j$  are the species masses. Inequality (14) represents a fundamental transition point in the dimensionless parameter space that describes edge instabilities in the presence of an X-point. Similar to the arguments put forward by Connor and Taylor,<sup>25</sup> this condition can be expected to indicate a change in behavior of the system without a detailed knowledge of the solutions of the model, or even the physical processes. The condition arises solely from scaling analysis and the assertion that resistive modes of the type described by Eqs. (1) – (4) and X-point physics are important ingredients.

We speculate that the observed QC mode is probably the lowest-k RX-EM mode that remains disconnected. The low value of  $k$  enhances transport ( $D \sim \gamma/k^2$ ) across the separatrix that is critical to the EDA regime. In addition to linear instability drive, the observed mode may be fed by inverse cascade from an unstable higher-k RX-ES spectrum. The emergence of a single mode, for parameters not sufficient to drive fully developed pressure-gradient driven (RB) turbulence, has been noted in previous nonlinear model computations.<sup>26</sup>

### ***B. Qualitative comparison with experiment***

Rewritten in terms of plasma parameters, Eq. (14) becomes

$$5.5 \times 10^{-7} \frac{(L_n / \rho_{\theta i}) f_{\text{mhd}}^2 q^2 n_e^{1/2}}{(a/R) T^2} > 1 \quad (15)$$

where dimensional units are again employed:  $n_e(\text{cm}^{-3})$ ,  $T_e = T_i = T(\text{eV})$ . Here  $\rho_{\theta i} = \rho_i B/B_\theta$  is the poloidal Larmor radius,  $a/R$  is the tokamak inverse aspect ratio, and we have set  $\omega_a = v_a/qR$  and  $\gamma_{\text{mhd}}^2 = f_{\text{mhd}}^2 c_s^2 (RL_n)$ . The extra dimensionless order unity form factor  $f_{\text{mhd}}$  [not present in Eq. (14)] will be used to fit the hand-waving MHD stability limit  $Y = 1$  to more realistic experimental values.

The parameter scalings of (15) have several points of qualitative agreement with experiments.<sup>1-3</sup> First, for typical EDA regime parameters near the separatrix where the mode should locate, the left-hand-side is unity in order-of-magnitude. Illustrative edge parameters are  $f_{\text{mhd}} = 2$ ,  $L_n = 0.4 \text{ cm} \approx \rho_{\theta i}$ ,  $n_e = 10^{14} \text{ cm}^{-3}$ ,  $q = 3.5$ ,  $T = 40 \text{ eV}$ ,  $a/R = 0.26$  and  $B = 4.2 \times 10^4 \text{ G}$ . The proposed condition (15) for the existence of a strong QC mode, and hence for the EDA regime, favors high  $q$ , larger  $L_n$  (than “ELMy H-mode”), and weakly favors larger  $n_e$ , all consistent with the experimental results reported in Ref. 1. The strong inverse scaling with  $T$  in Eq. (15) is consistent with the observation that the EDA regime favors higher neutral gas (i.e. lower edge  $T$ ).

In addition to the preceding, and in agreement with certain aspects of previously noted BOUT simulations,<sup>24</sup> the expected properties of the QC mode are consistent with experimental observations in several respects. The RX-EM mode has an electromagnetic component in the theory, as observed for the QC mode. The QC mode is observed in experiments *at the top and bottom* as well as on outboard side of the torus. This is consistent with a curvature driven mode like the RX mode (which penetrates up to the X-points) but not with strong RB modes (which are localized to the outboard midplane).

The experiments also show high-frequency broadband turbulence in addition to the QC mode, which is consistent with the higher- $k$  RX-ES spectra in the regime diagram. Furthermore, the high-frequency broadband turbulence is reported to get larger in L-mode (consistent with instability of the entire RX-ES and stronger RB branch).

While these correspondences between the theory and experiment are encouraging, there is also a possible weakness in the proposed hypothesis. The RX-EM/ES boundary ( $X=Y$ ) which gives the EDA regime is somewhat fragile in the theory, in that it is sensitive to the form of the X-point boundary condition that is employed (WKB vs. Born limit). The Born limit is explored in Appendix A where it is shown that the details of the growth rate scalings and RX-EM/ES regime transition boundary is sensitive to the form of the parallel shear profile  $k_{\perp}(s)$  in the Born limit. In some cases the RX-EM regime even disappears entirely. It remains an open question as to whether this fragility indicates a weakness in the theoretical hypothesis proposed here, or whether it perhaps merely indicates a sensitivity of EDA-like modes to details of the magnetic flux geometry.

A final point requiring further investigation is that the present theory [specifically Eq. (6) near maximum growth] predicts a mode frequency  $\text{Re}(\omega) \approx \omega_{*i}/2$  in the  $\mathbf{E} \times \mathbf{B}$  drift frame. Experimentally, the QC mode is observed to be in the  $\omega_{*e}$  direction *in the lab frame*. A reconciliation will require a self-consistent estimate of the resulting radial electric field ( $E_r$ ) well and comparison of the prediction with the observed toroidal rotation.

### ***C. Radial mode structure of the QC mode***

In addition to the generic scaling arguments made so far, the described method of treating RX modes can also be employed to obtain a model equation for their radial mode structure. Making the identification  $\mathbf{k}_{\perp} \rightarrow -i\mathbf{e}_x \partial/\partial x + k_y \mathbf{e}_y$ , and noting that a careful treatment of  $\gamma_{\text{mhd}}^2$  shows it to be proportional to  $k_y^2/k_{\perp}^2$  (see e.g. Ref. 7), the RX mode dispersion relation of Eq. (5) takes the form

$$\frac{\partial^2 \phi}{\partial x^2} - k_y^2 \left( 1 + \frac{\gamma_{\text{K}}^2}{F} \right) \phi = 0 \quad (16)$$

$$\gamma_{\kappa}^2 = -\frac{2}{m_i n_e R} \frac{\partial p}{\partial x} \equiv \gamma_{\text{mhd}}^2 \frac{k_{\perp}^2}{k_y^2} \quad (17)$$

$$F = \omega(\omega - \omega_{*i}) + i\omega_a \left( \frac{\omega(\omega - \omega_{*i})(\omega - \omega_{*e})}{\omega - \omega_{*e} + i\omega_{\eta}} \right)^{1/2} \rightarrow i\omega_a \omega \quad (18)$$

Here, the final form of  $F$  is the low- $k$  outgoing Alfvén wave limit.

Equation (16) has been solved numerically, using illustrative experimental parameters, and furthermore taking  $k_y$  from the data. (We will return to this point later.) In obtaining the solution, proper account must be taken of the appropriate branch of the square root to insure a legitimate outgoing-evanescent wave along the field line by monitoring  $\text{Im}(k_{\parallel})$ . The resulting radial mode structure is shown together with the assumed radial density profile in Fig. 3 a). Parameters for this case (at the top of the pedestal, denoted by subscript ped) are  $n_{\text{ped}} = 4 \times 10^{14} \text{ cm}^{-3}$ ,  $T_{\text{ped}} = 200 \text{ eV}$ ,  $B = 4.2 \times 10^4 \text{ G}$ ,  $R = 85 \text{ cm}$ ,  $q = 3.5$ ,  $L_{\parallel} = q R$ ,  $\mu = 2$  (i.e.  $m_i = 2 \text{ amu}$ ),  $Z = 1$ , and  $k_y = 4 \text{ cm}^{-1}$ . For the illustrated profile,  $L_n \sim 0.4 \text{ cm}$  at its minimum near the inflection point. The mode is seen to span the separatrix (where the separatrix location is assumed based on the shape of the density profile), and is localized near the maximum of  $\nabla p/p$  where  $p = nT$ . Furthermore, the mode is at the collisional RX-EM/ES regime boundary on the separatrix as shown Fig. 3 b) from the radial variation of  $\omega_{\eta}/\omega$ . Recall that  $\omega = \omega_{\eta}$  defines this regime boundary.

The present model is not adequate to predict the observed  $k_y$ . It is straightforward to show analytically [e.g. taking a “sharp boundary” limit of Eq. (16) to obtain radial matching conditions connecting the solutions on either side of the jump] that the RX-EM growth rate  $\gamma \propto k_y$  for  $k_y \rightarrow 0$  in our model. However, in reality, the mode will violate the disconnection condition, Eq. (8) or (9) first, making Eq. (16) inappropriate. Once connected, the RX-EM mode can “see” good curvature inside the separatrix on the HFS. This should provide a strong stabilizing influence. So the observed  $k_y$  may come from

the disconnection condition, which depends on details of the X-point magnetic geometry not considered here. The nonlinear inverse cascade, which pumps energy into the low-k modes, may also play a role in determining the observed  $k_y$ .

## V. Edge phase space diagram and the EDA regime

In Sec. IV A the natural wavenumber scale  $k_* = \omega/v_{*i}$  was used to eliminate  $k_\perp$  from the regime boundary describing the RX-EM/ES transition. Here, we apply the same philosophy to all the regime boundaries of Fig. 2, in order to systematically describe the edge parameter space.

With FLR physics, Eq. (1), or Eqs. (2) – (4) depend on the characteristic frequencies  $\omega_\eta$ ,  $\gamma_{\text{mhd}}$ ,  $\omega_a$ , and  $\omega_{*i}$ , from which we can arbitrarily choose three dimensionless combinations:  $\omega_\eta\gamma_{\text{mhd}}/\omega_a^2$ ,  $\gamma_{\text{mhd}}^2/\omega_a^2$  and  $\omega_{*i}/\gamma_{\text{mhd}}$ . These, however, still depend on  $k$ . Motivated by Ref. 12, we can choose a characteristic  $k$  relevant to the RB boundary defined by  $\omega_\eta\gamma_{\text{mhd}} \sim \omega_a^2$  (viz.  $XY^{1/2} \sim 1$ ) and then use this  $k$  in  $\omega_{*i}/\gamma_{\text{mhd}}$  to measure the strength of FLR stabilization. We thus obtain the two phase space parameters

$$\alpha_{\text{mhd}} = \frac{\gamma_{\text{mhd}}^2}{\omega_a^2} \quad (19)$$

$$\alpha_{\text{d}} = \frac{v_{*i}\omega_a}{\delta_e v_e^{1/2} \gamma_{\text{mhd}}^{3/2}} \quad (20)$$

where recall that  $\alpha_{\text{mhd}} \equiv Y$  measures the strength of MHD curvature drive relative to line bending. These are essentially the parameters defined in Ref. 12, up to order unity constants, and distinctions between the various possible scale lengths of density, pressure, etc.

The procedure is to set the growth rate at each of the regime boundaries of Fig. 2 to  $\omega_{*i}$  and thereby obtain the critical  $k_*$  at which FLR stabilization becomes dominant.

Then this  $k_*$  is employed in  $X \equiv \omega_\eta/\omega_a$  to express the function form of the boundary  $Y(X)$  in terms of the parameters  $\alpha_{\text{mhd}}$  and  $\alpha_d$ .

To alleviate the tedium of these calculations it is useful to note (after some algebra) that

$$C^{1-2\alpha} \alpha_{\text{mhd}}^{\mu(1-2\alpha)-2\beta+3/2} \alpha_d^2 < 1 \quad (21)$$

is the condition that a mode on the boundary  $X = CY^\mu$  is unstable (i.e.  $k < k_*$  so it is not FLR stabilized) where the normalized growth rate of the mode in question on the boundary is  $\hat{\omega} = X^\alpha Y^\beta$ . (When the growth rate is continuous across the boundary, the scaling on either side may be used.)

Results are summarized in Table 4 and, schematically, in Fig. 4. The labels in Fig. 4 indicate the types of modes that are unstable in each of the parameter space regimes. The label RX implies instability of both the RX-EM and RX-ES branches. At the far left of the diagram ( $\alpha_d \ll 1$ ) there is no FLR stabilization and the RB branch is robustly unstable (as well as all the smaller  $k$  modes from Fig. 2 that are present at the given value of  $\alpha_{\text{mhd}} \equiv Y$ ). Nonlinear simulations<sup>12</sup> suggest the identification of this regime with L-mode. In the opposite limit,  $\alpha_d > 1$ , FLR effects are strong, and completely stabilize all curvature driven modes, provided  $\alpha_{\text{mhd}} < 1$ . In the upper-right corner of the diagram,  $\alpha_d, \alpha_{\text{mhd}} > 1$ , the plasma is unstable to ideal modes (down to small  $k$ , which are not effectively FLR stabilized). In this discussion, we regard  $\alpha_{\text{mhd}} < 1$  as representing an ideal stability condition, recognizing that several considerations outside the scope of the present treatment can be important in determining this boundary. Such considerations would include the bootstrap current<sup>27</sup> and second stability effects, as well as non-local diamagnetic physics.<sup>28</sup> Qualitatively, the picture up to this point is similar to that of Ref. 12.

X-point physics adds a new regime to the  $(\alpha_{\text{mhd}}, \alpha_{\text{d}})$  parameter space near the L-H boundary at intermediate  $\alpha_{\text{d}} \sim 1$  in the MHD stable regime ( $\alpha_{\text{mhd}} < 1$ ),

$$1 < \alpha_{\text{d}} < \frac{1}{\alpha_{\text{mhd}}^{1/4}} \quad (22)$$

in which the entire RX-EM spectrum and part of the RX-ES spectrum is unstable. This is the parameter range for the QC mode postulated in Sec. IV A, *viz.* Eq. (22) is equivalent to the condition that  $k_*$  lies in the RX-ES regime. Consequently, the regime identified by Eq. (22) and shown with thick boundaries in the sketch of Fig. 4 is postulated to be the EDA regime. Nonlinear simulations, beyond the scope of the present paper, would be required to map out the boundary of the EDA regime quantitatively. Finally, we note, that as the ideal stability limit is approached ( $\alpha_{\text{mhd}} \rightarrow 1$ ), the window for the EDA regime is predicted to shrink. This may relate to the experimental observation that EDA regime operation favors stably shaped plasmas,<sup>1</sup> at moderate  $\delta$  and high  $q_{95}$ .

## VI. Conclusions

We have developed an analytic theory of resistive curvature-driven modes in the edge region of a diverted tokamak and shown the inter-relationships, parameter regimes and growth rate scalings of the various types of modes that arise. These range from the conventional ideal ballooning and resistive ballooning modes which are localized near the midplane region to the resistive X-point and interchange modes which remain finite through (at least part of) the X-point region. The principal new results of the mode analysis of Secs. II and III are the analytic dispersion relation for resistive X-point modes in the WKB limit, Eq. (5), and the regime diagram of Fig. 2, showing the domains and scalings of the various modes with collisionality, wavenumber and strength of the curvature drive.

In addition to describing growth rates of linear instabilities, we also showed that a similar type of reasoning could be applied to deduce scalings for the radial convective velocity of blobs. The blob regimes and scalings are obtained from Fig. 2 and Table 3.

The preceding theory was also applied in Secs. IV and V to describe the quasi-coherent mode and EDA regime observed on C-Mod. In the present nomenclature, we postulate that the quasi-coherent mode is an electromagnetic resistive X-point mode (RX-EM). Analytical scalings for the existence of this mode were found to compare well with experimental trends for obtaining the EDA regime with edge safety factor, density and (inferred) temperature. The principal theoretical scalings are given in Eqs. (14) or (15). Similar to previous BOUT simulations of the QC mode, the qualitative features were found to agree with experimental observations regarding the electromagnetic character, and poloidal extent of the mode. Furthermore, a model radial eigenvalue problem for the QC mode was formulated and solved [Eq. (16)].

By introducing a wavenumber scale corresponding to the finite Larmor radius (diamagnetic) stabilization condition, and eliminating wavenumber from the mode instability regimes, an edge phase space diagram appropriate to divertor geometry was constructed. This is the final principle result of our paper, and is given in Fig. 4. It was found that X-point physics adds a new region to the  $(\alpha_{\text{mhd}}, \alpha_{\text{d}})$  edge parameter space that is postulated to be the enhanced D-alpha (EDA) regime. The predicted location of this regime is given by Eq. (22), which however, is only qualitatively accurate (up to order unity constants, and treating the ideal MHD stability boundary conceptually). Nonlinear simulations with flux surface shaping and divertor geometry will be required to elucidate the detailed transition boundaries in this edge parameter space.

## Acknowledgments

The authors wish to thank W. M. Nevins and X. Q. Xu for discussions of the physics of the quasi-coherent mode dating back several years, and including the possible role of the inverse cascade. We thank M. Umansky for more recent discussions and BOUT code simulation results. Conversations with J. Terry on C-Mod experimental observations are also gratefully acknowledged. This work was supported by the U.S. Department of Energy (DOE) under grant DE-FG02-97ER54392; however, such support does not constitute an endorsement by the DOE of the views expressed herein.

## Appendix A: Resistive X-point modes in the Born limit

### *X-point equation and method of solution*

In the X-point region we must solve Eq. (4) which takes the dimensionless form

$$\frac{d}{dz} \frac{h^2}{1 + ib^2 h^2} \frac{d\Phi}{dz} + h^2 d^2 \Phi = 0 \quad (\text{A1})$$

where we drop diamagnetic effects,  $\nabla_{\parallel} = d/ds$ ,  $z = s/L_g$  is a dimensionless parallel coordinate, with  $L_g$  an equilibrium parallel scale length,  $b^2 = \omega_{\eta 0}/\omega$ ,  $d = \omega/\omega_{ag}$ , and  $\omega_{ag} = v_a/L_g$ . In this appendix, for clarity we denote quantities at the entrance to the region with subscript 0.

The parallel spatial variation enters Eq. (A1) through  $h(z) = k_{\perp}/k_{\perp 0}$  which grows dramatically in the X-point region due to magnetic shear (and also poloidal field variation). We model this effect by considering two explicit profiles of  $h(z)$  in the following subsections.

Analytic solutions to Eq. (A1) are possible when  $d \gg 1$  (WKB limit, treated in the main text) or  $d \ll 1$  (Born limit) considered in this appendix. The Born method may

be briefly summarized as follows. For  $z, b \sim 1$ , we integrate Eq. (A1) neglecting  $h^2 d^2 \Phi$  to obtain an explicit solution. In the asymptotic regime  $z \gg 1$  we use  $h^2 d^2 \gg 1$  to solve for the evanescent branch at  $\infty$ , again in terms of explicit functions. The  $z \sim 1$  and  $z \gg 1$  solutions are then matched in an overlap region. Finally, it is then possible to calculate  $d \ln \phi / dz$  at the entrance to the X-point region ( $z = 0$ ) to get the desired boundary condition for use in Eq. (3).

***Parabolic profile of  $k_{\perp}^2(s)$***

The first profile we consider is the parabolic profile of  $k_{\perp}^2(s)$ ,

$$h(z) = (1 + z^2)^{1/2} \quad (\text{A2})$$

The  $h^2 d^2 \rightarrow 0$  limit of Eq. (A1) may be integrated to give

$$\Phi = C \arctan z + i b^2 C z + D \quad (\text{A3})$$

where  $C$  and  $D$  are constants of integration. The sub-limit of this solution for  $z > 1$  is therefore  $\Phi = (C\pi/2 + D) + iCb^2 z$ . Once  $C$  and  $D$  are determined, the desired logarithmic derivative at  $z = 0$  is

$$\left. \frac{1}{\Phi} \frac{d\Phi}{dz} \right|_{z=0} = \frac{C}{D} (1 + i b^2) \quad (\text{A4})$$

To obtain  $C$  and  $D$  we solve the  $z \gg 1$  limit of Eq. (A1), which takes the form

$$\frac{\partial^2 \phi}{\partial \xi^2} + i \xi^2 \phi = 0 \quad (\text{A5})$$

where  $\xi = z(bd)^{1/2} \sim 1$ . The solutions may be expressed in terms of either parabolic cylinder functions or Whittaker functions. The solution that is evanescent at infinity (check *a posteriori*) and regular at  $\xi = 0$  is

$$\Phi = U(0, x) = x^{-1/2} W_{0, -1/4}(x^2/2) \quad (\text{A6})$$

where  $x = 2^{1/2} \exp(-i\pi/8)\xi$  and we adopt the notation of Ref. 29. Taking the  $\xi \ll 1$  sub-limit of Eq. (A6) and matching to Eq. (A3) in their region of overlapping validity yields the ratio

$$\frac{C}{D} = \frac{(bd)^{1/2} C_\alpha}{C_\beta ib^2 - (\pi/2)(bd)^{1/2} C_\alpha} \quad (\text{A7})$$

where  $C_\alpha = (\pi/2)^{1/2} e^{i\pi 7/8} / [2 \Gamma(5/4)]$ ,  $C_\beta = (\pi/2)^{1/2} / \Gamma(3/4)$  and  $\Gamma$  is the gamma-function. Finally, the desired boundary condition for the midplane region (EM and ES) is obtained as

$$\left. \frac{1}{\Phi} \frac{d\Phi}{dz} \right|_{z=0} = -ie^{i\pi 7/8} \frac{\Gamma(3/4)}{2\Gamma(5/4)} (1 + ib^2) \left( \frac{d}{b^3} \right)^{1/2} \quad (\text{A8})$$

Combining with Eqs. (2) and (3) of the main text we obtain the dispersion relation

$$\gamma_{\text{mhd}}^2 - ie^{i\pi 7/8} \frac{\Gamma(3/4)\omega_a \omega_{\text{ag}}^{1/2} \omega^{5/4}}{\Gamma(5/4)\omega_{\eta 0}^{3/4}} = 0 \quad (\text{A9})$$

Note that Eq. (A9) has employed  $\omega \ll \gamma_{\text{mhd}}$ , valid for the RX regime. The resulting RX mode growth rate is given by

$$\omega = A_0 \frac{\gamma_{\text{mhd}}^{8/5} \omega_{\eta 0}^{3/5}}{\omega_a^{4/5} \omega_{\text{ag}}^{2/5}} \quad (\text{A10})$$

where the constant  $A_0$  arises from the branch cuts, and implies unstable roots for the three choices  $A_0 = \{\pm 0.75 + 0.24i, 0.79i\}$ . Equation (A10) is to be compared with the WKB result (taking  $\omega_* = 0$ ) of Eqs. (6) or (7). We note that the parabolic profile result shows no structural or growth rate scaling change between the ES and EM limits ( $b \gg 1$  and  $b \ll 1$  respectively) because the factor  $(1 + ib^2)$  in Eqs. (A8) and (3) cancels out.

### ***Exponential profile of $k_\perp(s)$***

A similar analysis may be carried out for the exponential profile

$$h(z) = \exp(z) \quad (\text{A11})$$

Following the same procedure as for the parabolic case, the  $h^2 d^2 \rightarrow 0$  limit yields  $\Phi = C[\text{ib}^2 z - \exp(-2z)/2] + D$ . The large  $z$ ,  $h$  limit gives Bessel's equation, and the evanescent solution at infinity is  $\Phi = K_0(\xi)$  where here  $\xi = bd \exp(-i\pi/4 + z)$ . After matching these two solutions in their region of overlapping validity, we obtain the desired result

$$\frac{1}{\Phi} \left( \frac{d\Phi}{dz} \right)_0 = \frac{-2(1 + \text{ib}^2)}{1 + 2i\alpha_c b^2} \quad (\text{A12})$$

where  $\alpha_c = \ln 2 - \gamma_E - \ln \xi_0$  and  $\gamma_E$  is Euler's constant.

The resulting RX mode dispersion relation is

$$\gamma_{\text{mhd}}^2 - \frac{4\omega_a \omega_{\text{ag}}}{1 + 2i\alpha_c b^2} = 0 \quad (\text{A13})$$

and the RX mode growth rate for the exponential profile is

$$\omega = \frac{2i\alpha_c \omega_\eta \gamma_{\text{mhd}}^2}{4\omega_a \omega_{\text{ag}} - \gamma_{\text{mhd}}^2} \approx \frac{i\alpha_c \omega_\eta \gamma_{\text{mhd}}^2}{2\omega_a \omega_{\text{ag}}} \quad (\text{A14})$$

The last approximation is normally valid, since  $Y \ll 1$  is required to avoid the stronger ideal unstable (IB) branch. This typically implies  $\gamma_{\text{mhd}}^2 \ll \omega_a \omega_{\text{ag}}$  (unless  $L_g \gg L_\parallel$ ). In the same limit, we see that  $\omega/\omega_{\eta 0} \ll 1$  so the mode is necessarily electrostatic. In the opposite limit,  $\gamma_{\text{mhd}}^2 \gg \omega_a \omega_{\text{ag}}$  the mode is damped. Thus there is no RX-EM mode for an exponential profile, only RX-ES modes.

### ***Transition between the WKB and Born limits***

In the ES limit ( $\omega_\eta \gg \omega$ , or  $b \gg 1$ ) we can solve Eq. (A1) for the exponential profile exactly, yielding the same Bessel solution as in the preceding discussion,  $\Phi = K_0(\xi)$ . This otherwise general result elucidates the transition between the WKB and Born limits.

The desired boundary condition for the midplane region is

$$\frac{1}{\Phi} \frac{d\Phi}{dz} \Big|_{z=0} = -\xi_0 \frac{K_1(\xi_0)}{K_0(\xi_0)} \quad (\text{A15})$$

where  $\xi_0 = e^{-i\pi/4} b d$ . The RX mode dispersion relation is

$$\gamma_{\text{mhd}}^2 \pm \frac{\omega_a \omega^{3/2} e^{i\pi/4}}{\omega_{\eta 0}^{1/2}} \frac{K_1(\xi)}{K_0(\xi)} = 0 \quad (\text{A16})$$

The WKB sub-limit is  $\xi_0 \sim k_{\parallel} L_g \gg 1$  while the Born sub-limit is  $\xi_0 \ll 1$ .

Expanding the Bessel ratio in large and small argument limits, we find

$$\frac{1}{\Phi} \nabla_{\parallel} \Phi \sim \begin{cases} ik_{\parallel} \equiv 1/\lambda_{\parallel} & \xi_0 \gg 1 \\ -1/\alpha_c L_g & \xi_0 \ll 1 \end{cases} \quad (\text{A17})$$

In the WKB limit ( $\lambda_{\parallel} < L_g$ ) the mode “sees” into the X-point region a distance equal to its evanescence length  $\lambda_{\parallel}$ , whereas in the Born limit ( $L_g < \lambda_{\parallel}$ ) the mode sees into the X-point region a distance equal to the equilibrium scale length  $L_g$ . Thus in the WKB limit, the dispersion relation only “knows” about conditions at the entrance to the X-point region, while in the Born limit it “knows” about conditions further in.

### *Appendix summary*

The main conclusion from this appendix is that RX modes exist when the magnetic geometry variation along B is both gentle (WKB limit of the main text) and rapid (Born limit). The growth rate scalings are slightly different in each case. Depending on the details of the profile in the Born limit, the RX-EM subtype may not exist. This situation occurred for the exponential profile example, and may be a general feature of cases with very rapidly increasing profiles of shear in the parallel direction.

## References

1. M. Greenwald, R. Boivin, P. Bonoli, R. Budny, *et al.*, Phys. Plasmas **6**, 1943 (1999).
2. J.A. Snipes, Plasma Phys. Control. Fusion **43**, L23 (2001).
3. J.L. Terry, N.P. Basse, I. Cziegler, M. Greenwald, *et al.*, in *Proceedings of the 20th IAEA Fusion Energy Conference*, Faro, Portugal, 2004 (International Atomic Energy Agency, Vienna, 2005), paper IAEA-CN-116/EX/P4-12.
4. D.L. Rudakov, J.A. Boedo, R.A. Moyer, S. Krasheninnikov, *et al.*, Plasma Phys. Control. Fusion **44**, 717 (2002).
5. D. Farina, R. Pozzoli and D.D. Ryutov, Nucl. Fusion **33**, 1315 (1993).
6. J.R. Myra, D.A. D'Ippolito, X.Q. Xu and R.H. Cohen, Phys. Plasmas **7**, 2290 (2000).
7. J.R. Myra, D.A. D'Ippolito, X.Q. Xu and R.H. Cohen, Phys. Plasmas **7**, 4622 (2000).
8. X.Q. Xu, R.H. Cohen, T. D. Rognlien and J. R. Myra, Phys. Plasmas **7**, 1951 (2000).
9. T.C. Hender, B.A. Carreras, W.A. Cooper, J.A. Holmes, P.H. Diamond and P.L. Similon, Phys. Fluids **27**, 1439 (1984); and refs. therein.
10. R. J. Hastie, J. J. Ramos, and F. Porcelli, Phys. Plasmas **10**, 4405 (2003).
11. D.D. Ryutov and R.H. Cohen, Contrib. Plasma Phys. **44**, 168 (2004).
12. B.N. Rogers, J.F. Drake and A. Zeiler, Phys. Rev. Lett. **81**, 4396 (1998).
13. J.R. Myra, D. A. D'Ippolito and X.Q. Xu, Phys. Plasmas **9**, 1637 (2002).
14. P. B. Parks, W. D. Sessions, and L. R. Baylor, Phys. Plasmas **7**, 1968 (2000).
15. S.I. Krasheninnikov, D.D. Ryutov, and G.Q. Yu, J. Plasma Fusion Res. **6**, 139 (2005).

16. D. A. Russell, D. A. D'Ippolito, J. R. Myra, W. M. Nevins, and X. Q. Xu, *Phys. Rev. Lett.* **93**, 265001 (2004).
17. A.V. Nedospasov, V.G. Petrov, and G.N. Fidel'man, *Nuclear Fusion* **25**, 21 (1985);  
A.V. Nedospasov, *Fiz. Plazmy* **15**, 1139 (1989) [*Sov. J. Plasma Phys.* **15**, 659 (1989)].
18. S. I. Krasheninnikov, *Phys. Lett. A* **283**, 368 (2001).
19. D. A. D'Ippolito, J. R. Myra, and S. I. Krasheninnikov, *Phys. Plasmas* **9**, 222 (2002).
20. D. A. D'Ippolito, J. R. Myra, D. A. Russell, S. I. Krasheninnikov, A. Yu Pigarov, G. Q. Yu, X. Q. Xu, and W. M. Nevins, in *Proceedings of the 20th IAEA Fusion Energy Conference*, Faro, Portugal, 2004 (International Atomic Energy Agency, Vienna, 2005), paper IAEA-CN-116/TH/P6-2.
21. S.I. Krasheninnikov, A.I. Smolyakov, G. Yu, and T.K. Soboleva, *Czech. J. Phys.* **55**, 307 (2005).
22. G. Q. Yu and S. I. Krasheninnikov, *Phys. Plasmas* **10**, 4413 (2003).
23. J. R. Myra, D. A. D'Ippolito, S. I. Krasheninnikov, and G. Q. Yu, *Phys. Plasmas* **11**, 4267 (2004).
24. A. Mazurenko, M. Porkolab, D. Mossessian, J. A. Snipes, X. Q. Xu, and W. M. Nevins, *Phys. Rev. Lett.* **89**, 225004 (2002).
25. J.W. Connor and J. B. Taylor, *Phys. Fluids* **27**, 2676 (1984).
26. L. Garcia, B.A. Carreras and V.E. Lynch, *Phys. Plasmas* **9**, 47 (2002).
27. R.J. Groebner and T.H. Osborne, *Phys. Plasmas* **5**, 1800 (1998).
28. B.N. Rogers and J.F. Drake, *Phys. Plasmas* **6**, 2797 (1999).
29. *Handbook of Mathematical Functions*, eds. M. Abramowitz and I. A. Stegun, (Dover, New York, 1970), pp. 686, 687, 691.

## Tables

regime	growth rate $\hat{\omega} = \omega / \omega_a$	boundaries
IB	$Y^{1/2}$	$1, X^2 < Y$
RB	$Y^{1/2}$	$1/X^2 < Y < X^2$
RX-ES	$X^{1/3}Y^{2/3}$	$\epsilon_x^3 < X^2Y < 1$ $Y < X$
RX-EM	$Y$	$\epsilon_x^2 < XY$ $X < Y < 1$
C	$\frac{\omega_a}{\omega_s} Y$	$X^2Y < \epsilon_x^3$ if $Y < X$ $XY < \epsilon_x^2$ if $X < Y$ $Y < 1$

Table 1. Regime summary (WKB limit) where  $X = \omega_\eta/\omega_a$ ,  $Y = \gamma_{\text{mhd}}^2/\omega_a^2$ . The growth rate for C is an example for the sheath-connected collisionless limit.

	linea	blob
r		
	$k_\perp$	$1/a_b$
	$L_n$	$a_b$
	$\gamma$	$v_x/a_b =$ $c\phi/a_b^2B$
	$k_\parallel$	$1/L_\parallel$

Table 2. Correspondences between linear and blob parameters. The blob radius is  $a_b$ .

regime	description	$v_x$ (analytic)	$v_x$ (cm/s)
IB	ideal 3-D blob	$\frac{c_s a_b^{1/2}}{R^{1/2}}$	$6.9 \times 10^5 \frac{a_b^{1/2} T_e^{1/2}}{R^{1/2}}$
RB	local 2-D blob	$\frac{c_s a_b^{1/2}}{R^{1/2}}$	$6.9 \times 10^5 \frac{a_b^{1/2} T_e^{1/2}}{R^{1/2}}$
RX-ES	3-D resistive-disconnected blob	$\frac{q^{2/3} c_s \rho_s^{1/3} v_e^{1/3}}{a_b^{1/3} \Omega_e^{1/3}}$	$490 \cdot \frac{q^{2/3} n_e^{1/3} T_e^{1/6}}{a_b^{1/3} B^{2/3}}$
RX-EM	Alfvén-wave-emitting blob	$\frac{q c_s^2}{v_a}$	$3.1 \frac{q n_e^{1/2} T_e}{B}$
C	sheath-connected 2-D blob (collisionless limit)	$\frac{q c_s \rho_s^2}{a_b^2}$	$1.4 \times 10^{10} \frac{q T_e^{3/2}}{a_b^2 B^2}$

Table 3. Radial blob velocity scalings for WKB outgoing-evanescent wave conditions in the parallel direction. In the final column, the units are  $v_x$ (cm/s),  $n_e$ (cm<sup>-3</sup>),  $T_e$ (eV),  $a_b$ (cm),  $R$ (cm),  $B$ (G), and  $q = L_{||}/R$ . Numerical coefficients are approximate (order unity corrections may apply).

boundary	C	$\mu$	$\alpha$	$\beta$	instability condition
IB/RX-EM	1	$\infty$	0	1/2	$\alpha_{\text{mhd}} > 1$
RB/RX-ES	1	-1/2	0	1/2	$\alpha_{\text{d}} < 1$
RX-EM/RX-ES	1	1	0	1	$\alpha_{\text{mhd}} < 1/\alpha_{\text{d}}^4$
C/RX-EM	$\varepsilon_x^2$	-1	0	1	$\alpha_{\text{mhd}} > \varepsilon_x^{4/3} \alpha_{\text{d}}^{4/3}$
C/RX-ES	$\frac{\varepsilon_x^{3/2}}{2}$	-1/2	1/3	2/3	$\alpha_{\text{d}} < 1/\varepsilon_x^{1/4}$
IB/RB	1	1/2	0	1/2	$\alpha_{\text{mhd}} < 1/\alpha_{\text{d}}^2$

Table 4. Transformation of regime boundaries in (X, Y) space to ( $\alpha_{\text{mhd}}$ ,  $\alpha_{\text{d}}$ ) space using the diamagnetic stabilization condition. [see Eq. (21) for  $\mu \neq \infty$ ] Results for the C/RX-ES and C/RX-EM transitions are approached from the RX side of the boundary. Referring to Fig. 2, the inequality in the last column implies instability for modes on the indicated boundary, as well as all modes at the same Y with smaller k.

## Table captions

1. Regime summary (WKB limit). The growth rate for C is an example for the sheath-connected collisionless limit.
2. Correspondences between linear stability parameters and blob parameters. The blob radius is  $a_b$ .
3. Radial blob velocity scalings for WKB outgoing-evanescent wave conditions in the parallel direction. In the final column, the units are  $v_x(\text{cm/s})$ ,  $n_e(\text{cm}^{-3})$ ,  $T_e(\text{eV})$ ,  $a_b(\text{cm})$ ,  $R(\text{cm})$ ,  $B(\text{G})$ , and  $q = L_{\parallel}/R$ . Numerical coefficients are approximate (order unity corrections may apply).
4. Transformation of regime boundaries in  $(X, Y)$  space to  $(\alpha_{\text{mhd}}, \alpha_{\text{d}})$  space using the diamagnetic stabilization condition. [see Eq. (21) for  $\mu \neq \infty$ ] Results for the C/RX-ES and C/RX-EM transitions are approached from the RX side of the boundary. Referring to Fig. 2, the inequality in the last column implies instability for modes on the indicated boundary, as well as all modes at the same  $Y$  with smaller  $k$ .

## Figure captions

1. Schematic of current loops arising from the curvature-driven charge separation (current source). The topology of these current loops determines the edge regime.
2. Instability and blob transport regime diagram (WKB limit).
3. Radial mode structure of the QC mode: a) normalized density profile (dashed) and eigenfunction (solid) vs. radius, b) collisionality vs. radius.
4. Edge phase space diagram with X-points (WKB limit). Labels indicate the types of modes that are unstable in each of the parameter space regimes. RX implies instability of both the RX-EM and RX-ES branches. The regime bounded by the thick line is postulated to be the EDA regime.

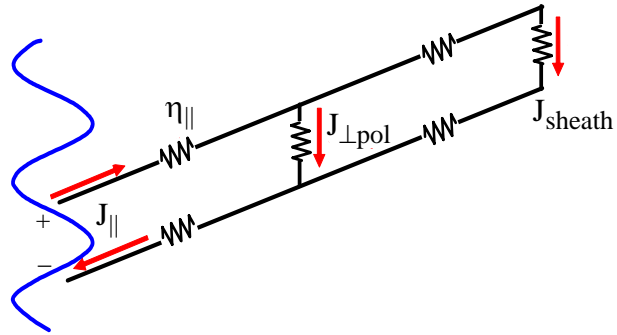


Fig. 1 Schematic of current loops arising from the curvature-driven charge separation (current source). The topology of these current loops determines the edge regime.

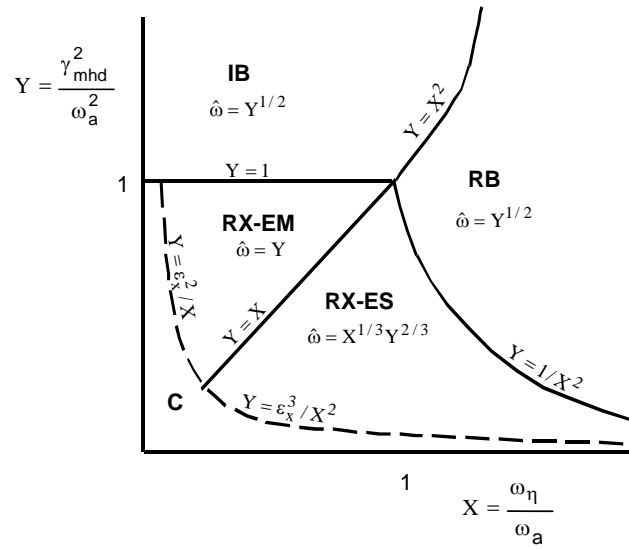


Fig. 2 Instability and blob transport regime diagram (WKB limit).

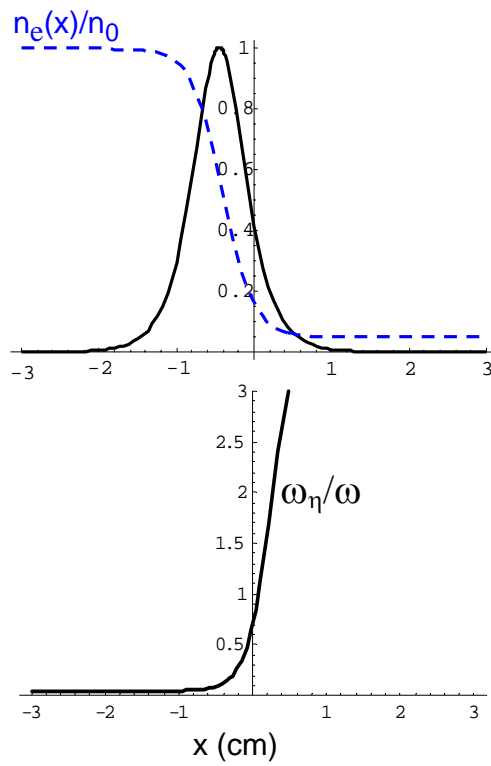


Fig. 3 Radial mode structure of the QC mode: a) normalized density profile (dashed) and eigenfunction (solid) vs. radius, b) collisionality vs. radius.

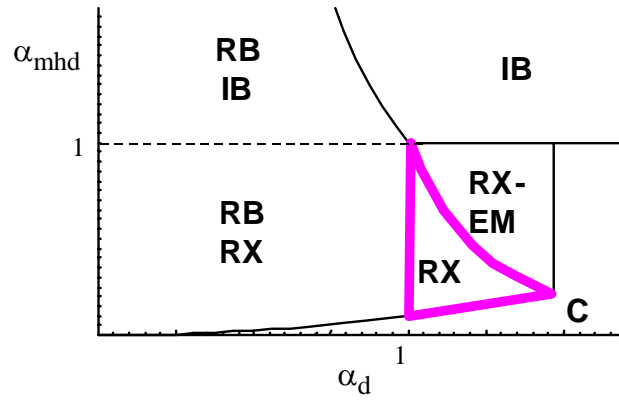


Fig. 4 Edge phase space diagram with X-points (WKB limit). Labels indicate the types of modes that are unstable in each of the parameter space regimes. RX implies instability of both the RX-EM and RX-ES branches. The regime bounded by the thick line is postulated to be the EDA regime.